Acta Materialia 167 (2019) 23–39

Contents lists available at ScienceDirect

Acta Materialia

journal homepage: www.elsevier.com/locate/actamat

Full length article

Deformation-driven bidirectional transformation promotes bulk nanostructure formation in a metastable interstitial high entropy alloy

Jing Su*, Xiaoxiang Wu, Dierk Raabe, Zhiming Li**

Max-Planck-Institut für Eisenforschung, Max-Planck-Str. 1, 40237, Düsseldorf, Germany

ARTICLE INFO

Article history:
Received 22 December 2018
Received in revised form
19 January 2019
Accepted 20 January 2019
Available online 23 January 2019

Keywords:
High entropy alloys
Deformation
Transformation
Nanostructure

ABSTRACT

We investigate the mechanisms of deformation-driven forward and reverse (bidirectional) martensitic transformation and the associated nanostructure formation in a metastable carbon-doped high entropy alloy (HEA) upon cold rolling. At thickness reductions below 14%, forward hexagonal-close packed (HCP) martensitic transformation prevails in the single face-centered cubic (FCC) matrix. Surprisingly, at the intersections of two crossing HCP lamellae, deformation-induced reverse transformation from the HCP martensite back to the FCC phase occurs. At higher thickness reductions around 26%–34%, multiple deformation kink bands develop, mainly on the pyramidal habit planes of the HCP martensite, among which reverted FCC phase is also observed resulting in a dual-phase nano-laminated structure. The deformation-induced reverted FCC phase regions exhibit a twin stacking sequence relative to the prior FCC matrix, which is related to the underlying dislocation reactions and rearrangement of the partial dislocations. At 67% thickness reduction, the deformation bands develop further into micro-shear bands consisting of nanosized (sub)grains. For rendering the dual-phase nanostructure back to single-phase FCC, 400 °C/10 min tempering is applied on a 34% cold-rolled specimen. The resulting nanostructure is characterized by nano-(sub)grains and nano-twins. It exhibits an excellent strength-ductility synergy (ultimate tensile strength 1.05 GPa at 35% total elongation) due to the improved work hardening enabled by both, FCC-HCP martensitic transformation in confined regions and mechanical twinning. With this, we show that bulk nanostructured alloys with bidirectional transformation can be designed by tuning the materials' phase stability to their thermodynamic limits with the aim to trigger sequential athermal forward and reverse transformation under load.

1. Introduction

With an ever-increasing demand for strong and ductile structural materials for weight-saving engineering applications, substantial efforts are devoted to developing new alloys and microstructures that enable beneficial properties. From a compositional perspective, high entropy alloys (HEAs) consisting of multi-principal elements have attracted attention in the past decade, opening up new pathways in tuning and exploiting massive solid-solution and athermal transformation phenomena [1,2]. Regarding the latter approach metastable HEAs such as non-equiatomic 50Fe-30Mn-10Co-10Cr (at. %) and interstitial carbon-doped 49.5Fe-30Mn-10Co-10Cr-0.5C (at. %) have shown improved mechanical properties compared to the more stable equiatomic CoCrFeMnNi reference HEA [3–7]. This is attributed to the widely tunable phase stability of such materials with the aim to utilize the associated deformation mechanisms including dislocation slip, stacking fault formation, deformation-induced martensitic phase transformation, and mechanical twinning. These deformation mechanisms can be activated jointly and/or sequentially to enhance the work hardening rate in those loading regimes where strain hardening reserves are needed to compensate for geometrical softening and strain localization [8].

From a microstructure perspective, efforts were invested in producing nanostructured alloys for achieving improvement in strength relative to their coarse-grained counterparts [9,10]. However, nano-grained materials typically show reduced tensile ductility at ambient temperature due to insufficient work hardening reserves. Yet, Lu et al. [11,12] demonstrated that nanostructures containing low-energy interfaces at the nanoscale can strengthen the material while preserving its ductility. Such low

* Corresponding author.
** Corresponding author.
E-mail addresses: j.su@mpie.de (J. Su), zhiming.li@mpie.de (Z. Li).

https://doi.org/10.1016/j.actamat.2019.01.030
1359-6454/

energy interfaces include twin boundaries [13], low angle grain boundaries (LAGBs) [14] and coherent phase boundaries [11]. It has been reported in a 316 L austenitic stainless steel [15] and a Cu–Al alloy [16] that nanostructures consisting of nano-twin lamellae and nano-sized grains inside shear bands can be synthesized by dynamic plastic deformation (DPD). Morikawa et al. [17] found similar nanostructures when cold rolling a 310S stainless steel to a thickness reduction of 70%. Typically such nanostructures form in face-centered cubic (FCC) structured metals with relatively low stacking fault energy (SFE, <40 mJ/m^2) in which mechanical twinning and shear banding are activated [16,18]. The interaction of shear bands with nano-twin lamellae can result in de-twinning inside the shear bands and formation of de-twinned dislocation substructures which eventually transform into nano-(sub)grains [16].

In the present study, we show that single FCC phase bulk nanostructures, characterized by nano-grains and nano-twins, can be realized in a metastable interstitial carbon-doped HEA (iHEA) by subjecting it to modest cold rolling (34%–67% reductions) and subsequent tempering (400 °C, 10 min). A surprising observation is that in this material not only the multiple well-known deformation mechanisms resulting from phase metastability such as martensitic phase transformation and twinning occur but also reverse transformations when exposed to loads. Particularly, the observation of a deformation-driven martensitic transformation from the original FCC host phase into the hexagonal close-packed (HCP) product phase and back is surprising. This means that the deformation-driven athermal transformation can be bidirectional, yet, in the form of different crystallographic variants. A recent study by Lu et al. [19] on a non-carbon doped metastable HEA has shown a similar effect. They reported the deformation-induced bidirectional transformation under uniaxial tensile loading at a quasi-static strain rate. It was found that the formation of reverted FCC phase from a preceding martensitic HCP region was related to the reverse motion of the Shockley partials that had been generated to form the HCP martensite. Here, a metastable carbon-doped iHEA has been chosen for studying, tuning and utilizing this bidirectional transformation induced plasticity (Bi-TRIP) effect to create bulk nanostructures.

The goal of this work is to investigate two phenomena: Firstly, we study the basic mechanisms associated with the bidirectional TRIP effect, viz. the deformation-induced forward and reverse martensitic transformation, the formation of micro-shear bands, as well as the associated dual-phase nano-structures that build up with increasing rolling strain. Secondly, we need to understand how these structures change upon 400 °C tempering, focusing on the restoration of a single FCC nanostructured phase via a thermally driven reverse phase transformation. The resulting work hardening behavior and the mechanical properties are also investigated. The study thus introduces a novel approach for producing strong and ductile bulk nanostructured metallic materials through a bidirectional martensitic phase transformation mechanism that can be triggered by a conventional rolling procedure.

2. Experimental

A non-equiatomic iHEA with nominal composition 49.5Fe-30Mn-10Co-10Cr-0.5C (at. %) was chosen for the study. The chemical composition of the as-cast iHEA has been reported elsewhere [8]. The as-cast alloy was hot rolled at 900 °C to a thickness reduction of 50% and then homogenized at 1200 °C for 2 h in an Ar atmosphere followed by water quenching. Cold rolling of the as-homogenized iHEA was conducted to thickness reduction ratios ranging from 14% up to 67%. The thickness reduction in each pass was ~0.5 mm at sheet thicknesses above 3 mm and ~0.2 mm for thicknesses below 3 mm. The effective logarithmic (true) strain was calculated according to the equation, $\varepsilon_f = \ln\left(\frac{H}{h}\right)$, where H and h are the initial and final thickness of the rolling plate, respectively [20]. Post-deformation tempering was performed at 400 °C for 10 min to recover the as-rolled microstructures followed by water quenching.

Digital image correlation (DIC) assisted uniaxial tensile tests were conducted at room temperature at an initial strain rate of 1×10^{-3}/s on the as-rolled and as-tempered specimens with thickness reductions of 34% and 67%, respectively. Nano-indentation mapping was performed using a Bruker Hysitron TriboScope under accelerating property mapping (XPM) mode to analyze the hardness response of specific microstructure features (e.g. regions containing high populations of nano-grains, dislocation cells, and nano-twins). A Berkovich shaped indenter was used with a maximum load of 2500 μN. Dilatometry was utilized to track thermally-induced phase transformation events at a heating rate of 10 K/s and a cooling rate of 50 K/s.

Microstructures were examined by scanning electron microscopy (SEM) using electron backscatter diffraction (EBSD) in a Jeol JSM-6500F SEM and electron channeling contrast imaging (ECCI) in a Zeiss Merlin SEM. Transmission-EBSD has been conducted on the Zeiss Merlin SEM at an accelerating voltage of 30 kV with a working distance of 2.6 mm and a step size of 7 nm. Phase analysis was carried out by X-ray diffraction (XRD) with a Meteor0D energy dispersive point detector and a Cobalt source operated at 40 kV and 30 mA. Substructures down to the atomic resolution were analyzed by transmission electron microscopy (TEM) using a Jeol 2200F and an FEI-TITAN at acceleration voltages of 200 kV and 300 kV, respectively. TEM thin foils were prepared via mechanical grinding followed by electro-polishing using a twin-jet polisher with the electrolyte solution consisting of 5% perchloric acid in 95% acetic acid. Elemental distribution analysis at the nanoscale was conducted by atom probe tomography (APT) using a LEAP 3000X HR, Cameca Inc. APT tips were prepared by focused ion beam (FIB) milling in an FEI Helio Nanolab 600i microscope.

3. Results

3.1. Microstructure evolution upon cold rolling

3.1.1. Bidirectional transformation at low thickness reduction (~14%)

The initial microstructure of the iHEA prior to cold rolling exhibits a single-FCC phase structure and equiaxed grains with an average size of ~65 μm. Fig. 1 presents the microstructure of the iHEA subjected to cold rolling to a low thickness reduction of 14%, which is equivalent to an effective (true) strain of 15%. At this stage, deformation-induced HCP martensitic transformation takes place in the FCC matrix. The HCP lamellae form parallel to the traces of {111} slip planes in the FCC matrix (Fig. 1a). The volume fraction of the HCP phase is ~20 vol % according to both XRD and EBSD analysis. In most of the grains, more than one slip systems can be activated and different HCP variants are observed. Interestingly, reversely transformed fresh FCC phase is detected at the intersections of two crossing HCP lamellae (Fig. 1c). This observation marks an important difference between the current iHEA transformation mechanism and the ones observed in martensitic steels [21,22]. For the current iHEA, surprisingly a fresh portion of FCC phase forms at these intersections, while in martensitic steels, body-centered cubic (BCC) or body-centered tetragonal (BCT) martensite is usually found at the intersections, according to the Olson-Cohen mechanism [23]. In some cases, it may also happen in steels that at such intersecting HCP lamellae no transformation

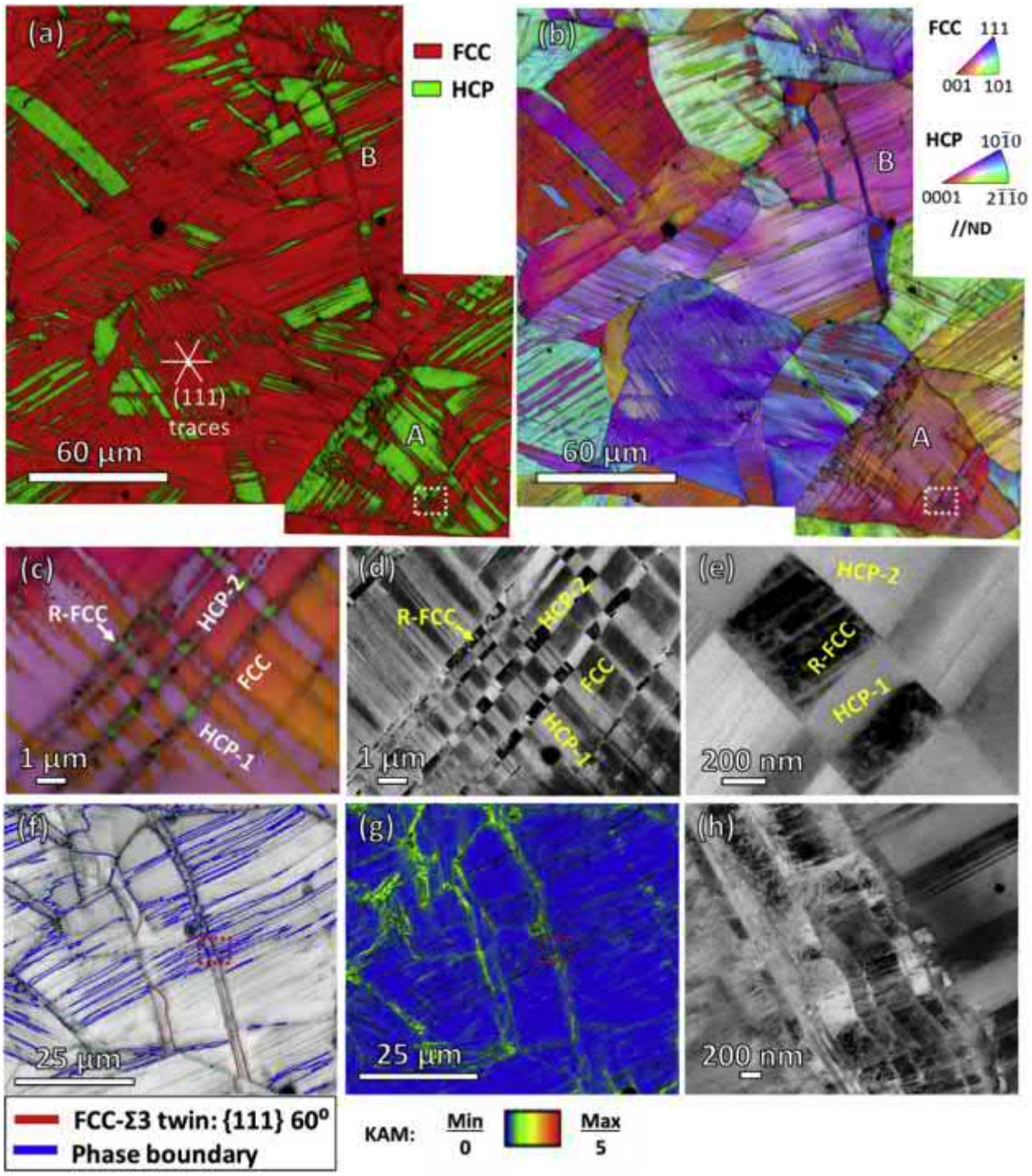

Fig. 1. As-rolled microstructure at a thickness reduction of 14%. (a) Phase map; (b) IPF map; (c) and (d) Enlarged IPF map and ECC image of the white rectangular region in grain 'A' showing two HCP variants and reverted FCC phase; (e) ECC image zooming in the reverted FCC phase revealing partial dislocations. (f) IQ map of grain 'B' overlapped with twin and phase boundaries; (g) KAM map showing higher KAM values along the deformation bands; (h) ECC image zooming in the red rectangular showing substructures inside the deformation band. (For interpretation of the references to colour in this figure legend, the reader is referred to the Web version of this article.)

occurs at all, yet, re-transformation back to FCC has rarely been reported to occur at such intersections. In the iHEA, the deformation-induced reverted FCC phase has a new orientation relative to the original FCC host matrix that it originally departed from (Fig. 1c). When zooming into the interaction area by ECC imaging, partial dislocations are observed in the reverted FCC phase (Fig. 1d and e).

Localized deformation bands are probed in grain 'B' (Fig. 1a, f-h). The deformation bands nucleate from the triple junctions of grain boundaries where the deformation is highly concentrated. In the kernel average misorientation (KAM) map (Fig. 1g), the deformation bands possess higher KAM values compared to the matrix grain. However, these deformation bands do not form along the {111} slip planes. They exhibit a misorientation angle of 60° with

respect to the matrix grain and a Σ3-twin relationship is partially identified along the deformation bands by EBSD analysis (red line in Fig. 1f). In the enlarged ECC image (Fig. 1h), multiple fine zigzag slip lines are observed inside the deformation bands interacting with the HCP lamellae.

3.1.2. Bidirectional transformation at medium reductions (26%–34%)

With increasing the thickness reduction from 14% to 26% (true strain from 15% to 30%), the volume fraction of the deformation-induced HCP martensite increases dramatically from ~20 vol% to ~60 vol% according to EBSD and XRD probing. As shown in Fig. 2a–c, deformation kink bands with thicknesses ranging from 100 nm to 500 nm initiate in the HCP phase. According to the trace analysis, it is found that the deformation kink bands mainly developed along the $\{11\bar{2}2\}$ pyramidal plane of the HCP phase (see white plane traces in Fig. 1a). Moreover, finer deformation bands along the $\{10\bar{1}1\}$ pyramidal plane trace are also found in the HCP lamellae (Fig. 2c_1). Alternating layers of HCP and FCC phases appear among the deformation bands (Fig. 2a and b). The deformation bands kink at the interfaces of HCP and FCC lamellae. In the partitioned IPF maps of the FCC and HCP phases (Fig. 2c_2 and c_3), the reverted FCC lamellae show a discontinuous morphology (Fig. 2c_2) mixed with the newly formed HCP variant (Fig. 2c_3). The new HCP variant shows a misorientation angle of 70.5° with respect to the primary HCP phase. In the ECC images (Fig. 2d and e), partial dislocations (marked by arrows) are observed in the reverted FCC lamellae and the {111} plane trace shows an angle of 70.5° relative to the {0001} plane of the forward transformed HCP martensite. This observation suggests that the new HCP martensite might have been transformed from metastable reverted FCC phase. This means that this region has undergone a trifold transformation during cold rolling, namely, from the original FCC host matrix to HCP, which in turn transformed to metastable FCC and again back into HCP.

At a thickness reduction of 34% (a true strain of 42%), the volume fraction of HCP martensite is more or less the same (~60 vol % according to EBSD and XRD analysis) compared to that at 26% reduction. This is related to the simultaneous occurrence of and the competition between the forward and reverse martensitic phase transformation, which will be discussed later in section 4.1.2. In Fig. 3a–c, deformation kink bands widely propagate, among which alternating layers of HCP phase and reverted FCC phase also appear. Inside the deformation bands, reversely transformed FCC phase is also observed (Fig. 3c_1). Many low angle grain boundaries (LAGBs) are identified inside the micro-shear bands, indicating the formation of nanosized subgrains (Fig. 3c_1 and c_2). Some deformation bands gradually grow into micro-shear bands with a thickness above 1 μm (indicated by the white arrows in Fig. 3a). In the remaining large FCC grains (Fig. 3d), mechanical twins are found co-existing with the HCP martensite lamellae along the same slip bands (blue and red lines refer to phase and twin boundaries, respectively). The {0001} and $\{10\bar{1}0\}$ pole figures of the HCP phase and the {111} and {100} pole figures of the FCC phase are given in Fig. 3f and g. The HCP phase shows a near-basal texture, although the {0001} plane normal tilts about 10° towards the rolling direction (RD) with respect to the normal direction (ND) of the rolling sheet. Accordingly, the $\{10\bar{1}0\}$ prismatic pole figure presents a fiber texture (Fig. 3f). Compared to the HCP phase, there is no obvious preferred crystallographic texture of the FCC grains, as the maximum intensities of the pole figures are low (Fig. 3g).

Fig. 4a–c demonstrate the activation of multiple slip systems and mechanical twinning in the HCP phase. Basal {0001}, prismatic $\{10\bar{1}0\}$, pyramidal I $\{10\bar{1}1\}$ and pyramidal II $\{11\bar{2}2\}$ slip traces are identified in the HCP grain (e.g., the grain I in Fig. 3a). The activation of non-basal slip systems is responsible for the basal pole splitting of the HCP texture as shown in Fig. 3f. Interestingly, tension twinning (89° and $\{10\bar{1}2\}$) is found in the HCP phase (marked by yellow lines in Figs. 3e and 4c), but contraction twins and secondary twins are rarely observed. Fig. 4d, e, and f illustrate the development of nano-(sub)grains inside the deformation bands at different stages by ECC imaging. In the newly formed deformation band with a thickness of around 150 nm in the HCP grain (e.g., the grain I in Fig. 3a), elongated nano-(sub)grains can be seen (Fig. 4d). In the well-developed deformation bands with a thickness of about 1 μm, (e.g., in grain II in Fig. 3a), elongated nano-(sub)grains gradually break up into more equiaxed nano-(sub)grains due to the large shear strain (Fig. 4e). In the bended micro-shear bands (e.g., in grain III in Fig. 3a), equiaxed nano-grains appear with the grain size ranging from 50 to 80 nm (Fig. 4f).

3.1.3. Formation of micro-shear bands and nanostructures at a high reduction (~67%)

Fig. 5 shows microstructure details of the iHEA subjected to 67% cold rolling (true strain 110%), together with the corresponding nano-indentation map. In the pseudo-3D-EBSD maps (Fig. 5a and b), numerous micro-shear bands propagate inside grains and across grain boundaries describing an S shape. The volume fraction of the HCP phase is ~67%, i.e. similar as for the 26% and 34% rolled specimens. However, the volume fraction of micro-shear bands largely increases (from ~10 vol % to ~35 vol %) as the thickness reduction increases from 34% to 67%. The nano-indentation map (Fig. 5c) shows that the shear band regions have a much higher hardness of ~7–8 GPa (marked by a white dashed line) compared to the grain interior (~5.5 GPa). This effect is due to the formation of nanostructures in the shear bands, as shown in Fig. 5d–f by TEM analysis. The enlarged bright field (BF) and dark field (DF) images (Fig. 5e and f) show that nano-grains with an average size of ~50 nm have formed inside the shear bands. Also, both HCP and FCC phase fractions appear inside the shear bands as revealed by selected area diffraction (SADP), Fig. 5g.

3.2. Development of single FCC nanostructures upon tempering

In order to recover the deformed microstructure and to trigger a thermally induced reverse transformation from the HCP martensite back to the FCC phase, tempering has been conducted at 400 °C for 10 min on the as-rolled specimens. Fig. 6 shows the tempered microstructure with a preceding rolling reduction of 67% as characterized by EBSD and ECCI. The corresponding nano-indentation map exhibits gradient hardness values at the grain scale (Fig. 6b). More specific, the center regions of the large grains show the lowest hardness value (~4.5 GPa), while the shear bands reveal the highest hardness level of 7–8 GPa associated with the formation of nano-grains (Fig. 6h). Regions adjacent to the shear bands have medium hardness value around 5.5–6 GPa. This can be ascribed to higher dislocation densities near the shear bands relative to the grain interior, as shown in the KAM map (Fig. 6c) and ECC images (Fig. 6f and g). The increase of the misorientation angle from point A to B and from C to D (Fig. 6d) also suggests that a larger lattice rotation appears near the shear bands where geometrically necessary dislocations (GNDs) accumulate to accommodate the local strain. In addition, twin lamellae appear bent in regions adjoining to the shear bands (shown in Fig. 6e) due to the larger shear strains compared to the grain interior. Overall, a single FCC phase nanostructure emerges after tempering characterized by complex hierarchal features including nano-twins (Fig. 6f) and submicron-sized dislocation cells adjacent to the shear bands (Fig. 6g) as well as nanocrystals inside the bands (Fig. 6h).

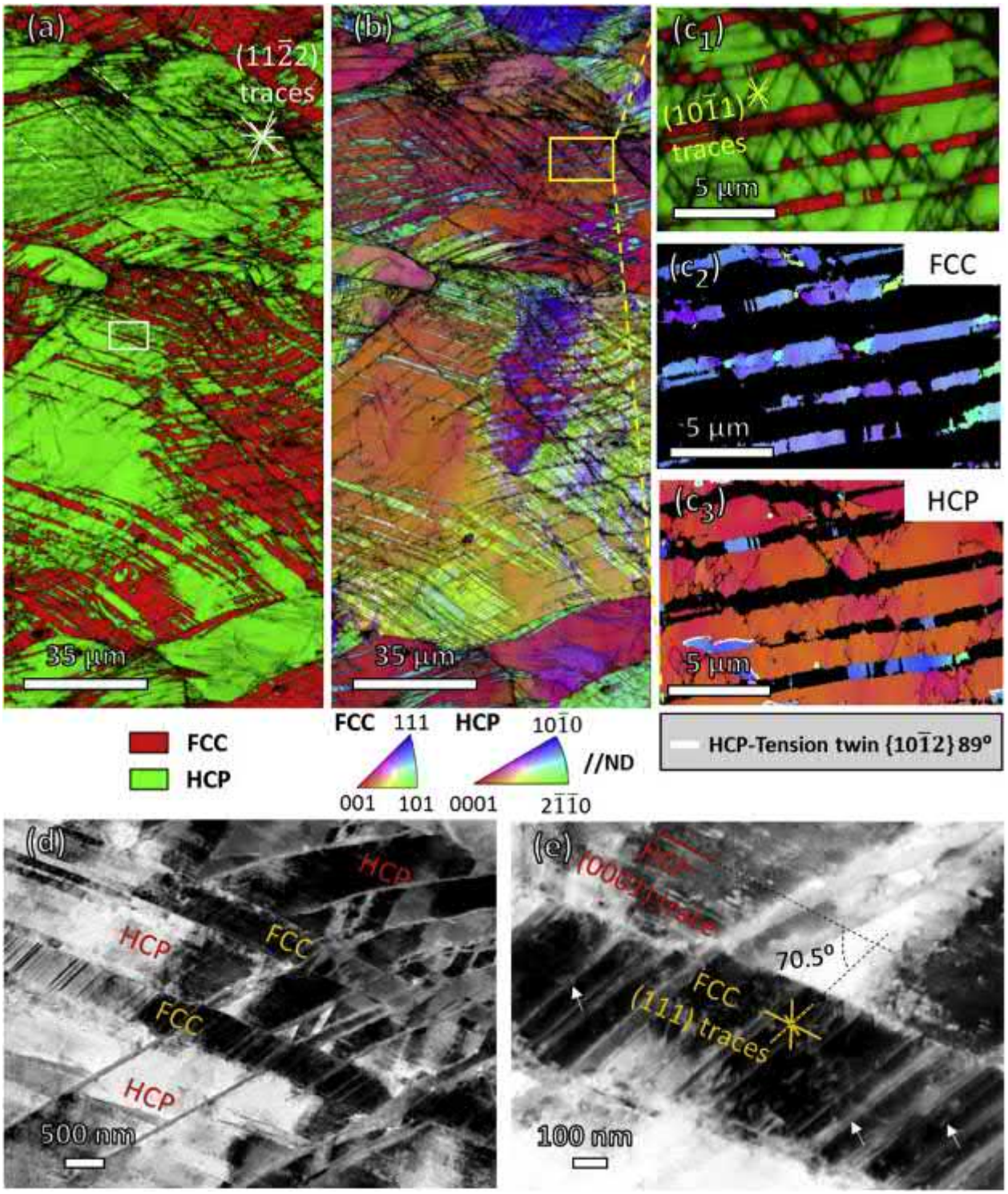

Fig. 2. As-rolled microstructure at a thickness reduction of 26%. (a) Phase map showing deformation kink bands in HCP phase developed along pyramidal II {11$\bar{2}$2} habit plane; (b) IPF map; (c_1) Enlarged phase map superimposed with IQ map of the yellow rectangular region in (b) revealing fine deformation bands along pyramidal I {10$\bar{1}$1} habit plane; (c_2) and (c_3) Partitioned IPF maps of FCC and HCP phases. (d) ECC image of the white rectangular region in (a) presenting alternating layers of HCP phase and reverted FCC phase; (e) Enlarged ECC image showing partial dislocations (pointed by white arrows) in the reverted FCC phase. (For interpretation of the references to colour in this figure legend, the reader is referred to the Web version of this article.)

3.3. Mechanical properties

The engineering stress-strain curves of the as-rolled specimens at thickness reductions of 34% and 67% as well as of the tempered specimens are compared in Fig. 7a. The corresponding true stress-true strain plots and the work hardening curves of the four samples are shown in Fig. 7b. The 67% rolled specimen shows a very high yield strength (YS) of 1.5 GPa and ultimate tensile strength (UTS) of 1.6 GPa, but limited total elongation of only 5%. After tempering, the strength is slightly reduced (YS, 1.3 GPa, and UTS, 1.5 GPa), whereas

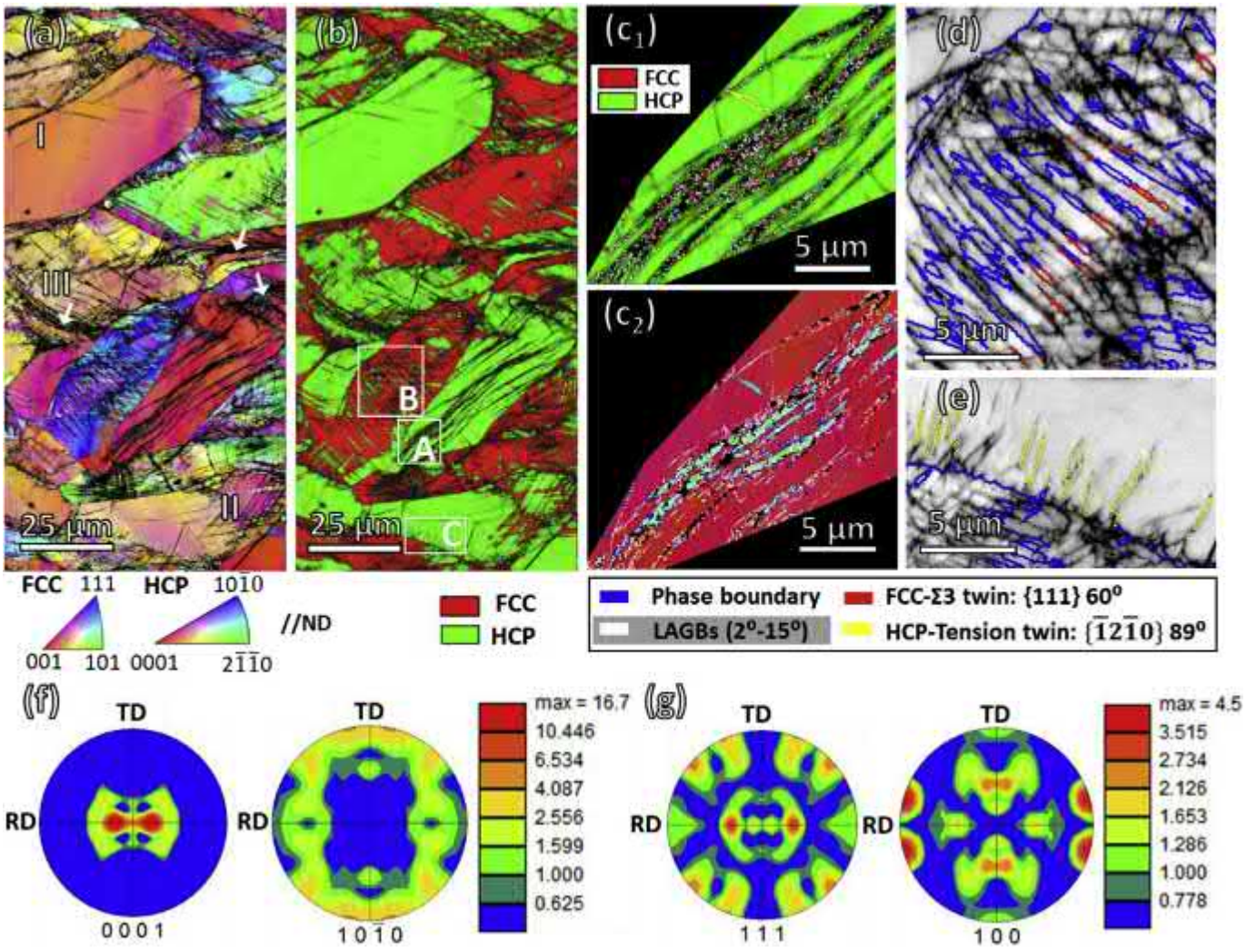

Fig. 3. As-rolled microstructure at a thickness reduction of 34%. (a) IPF map; (b) Phase map; (c_1) and (c_2) Enlarged phase map and IPF map of grain 'A' showing reverted FCC phase inside micro-shear bands; (d) IQ map of grain 'B' overlapped with twin and phase boundaries; (e) IQ map of grain 'C' showing the formation of extension twin in HCP phase. (f) {0001} and {10$\bar{1}$0} pole figures of the HCP phase; (g) {111} and {100} pole figures of the FCC phase.

the total elongation substantially increases to 14%. Yet, the uniform elongation values of the as-rolled and as-tempered samples are comparable, i.e. around 3%. This means that only the post-necking elongation is improved by tempering the 67% rolled material. This finding indicates that the corresponding work hardening rate of the tempered specimen is still not sufficiently high to prevent early necking.

Compared to the 67% rolled specimen, the sample subjected to 34% cold rolling reduction exhibits lower YS (1 GPa) and UTS (1.2 GPa), but its total elongation (~10%) is about twice as high. For the subsequently tempered specimen, YS and UTS decrease to 900 MPa and 1.05 GPa, respectively. However, the specimen's ductility is dramatically improved (total elongations of 35% at a uniform elongation of 14%). Fig. 8b shows that the work hardening rate of the tempered 34% rolled specimen is more pronounced than those of the other three samples. It is also worth mentioning that a slight increase of the strain-hardening rate appears at about 10% strain.

To understand the work hardening response and the underlying deformation mechanisms of the specimens with different initial nanostructures, the deformation microstructures of the tempered specimens with the pre-rolling reductions of 34% and 67% have been characterized at different local strains upon tensile loading (Figs. 8 and 9). Both specimens exhibit a single FCC phase structure prior to tensile testing. However, the nanostructures of the former consist of a lower fraction of micro-shear bands and thus a smaller amount of nano-(sub)grains (10% vs. 35%) compared to the latter (Fig. 9a). Fig. 8 shows the deformation microstructures at local strains of 10% and 30% of the tempered specimen with the preceding rolling reduction of 67%. Deformation-induced HCP martensite is barely observed at a local strain of 10% (Fig. 8a). The fraction of twins is counted as the length of the twin boundary over the scanning area (μm/μm^2). The fractions of the twins before tensile deformation and after 10% local strain are ~0.31 and ~0.32/μm, respectively. ECC imaging (Fig. 8d) reveals a new variant of nano-lamellae (twin or HCP) inside the large grains, although with a low volume fraction. This observation indicates that both, deformation-induced HCP phase transformation and mechanical twinning are largely inhibited. In the near-fracture region, the local strain is about 30% according to the local strain map taken by DIC analysis (Fig. 7c). It is found that shear bands lead to the formation of necking steps along the edge of the tensile specimen (Fig. 8e). On the fracture surface, micro-voids and cracks propagate along the shear bands (Fig. 8f and g).

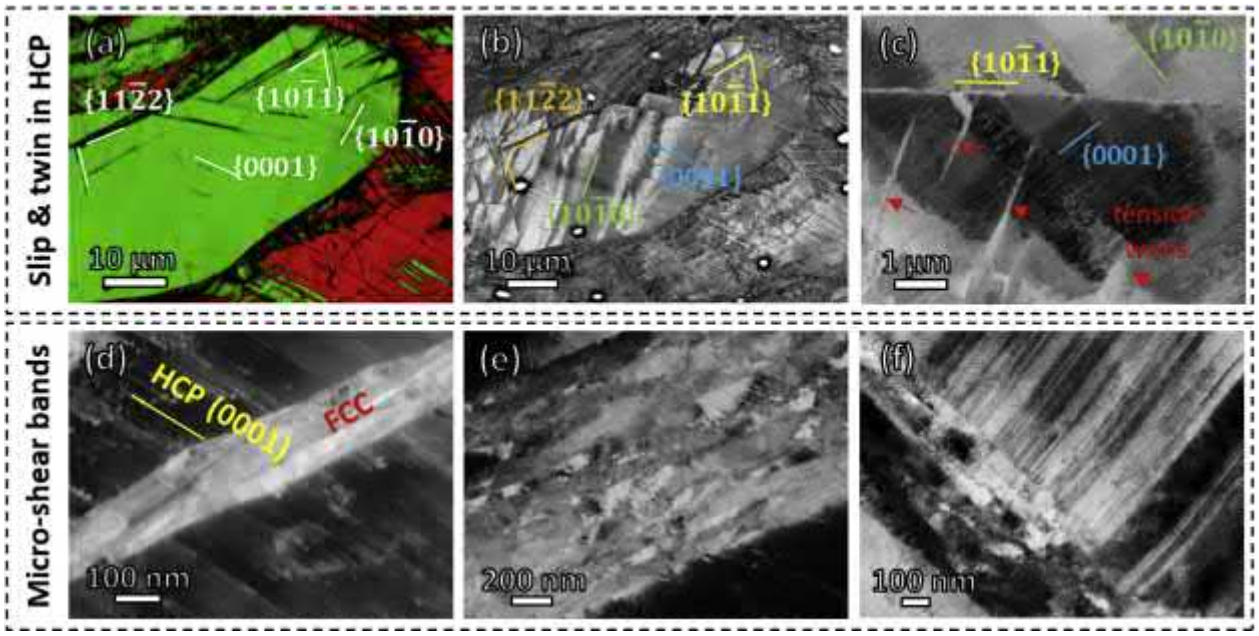

Fig. 4. Detailed substructures in the 34% rolled specimen. (a) Phase map; (b) ECC image revealing basal {0001}, prismatic {10$\bar{1}$0}, pyramidal I {10$\bar{1}$1} and pyramidal II {11$\bar{2}$2} slip traces in HCP phase; (c) ECC image showing tension twin and slip traces. (d), (e) and (f) ECC images demonstrating the formation of nano-(sub)grains in the micro-shear bands at different stages.

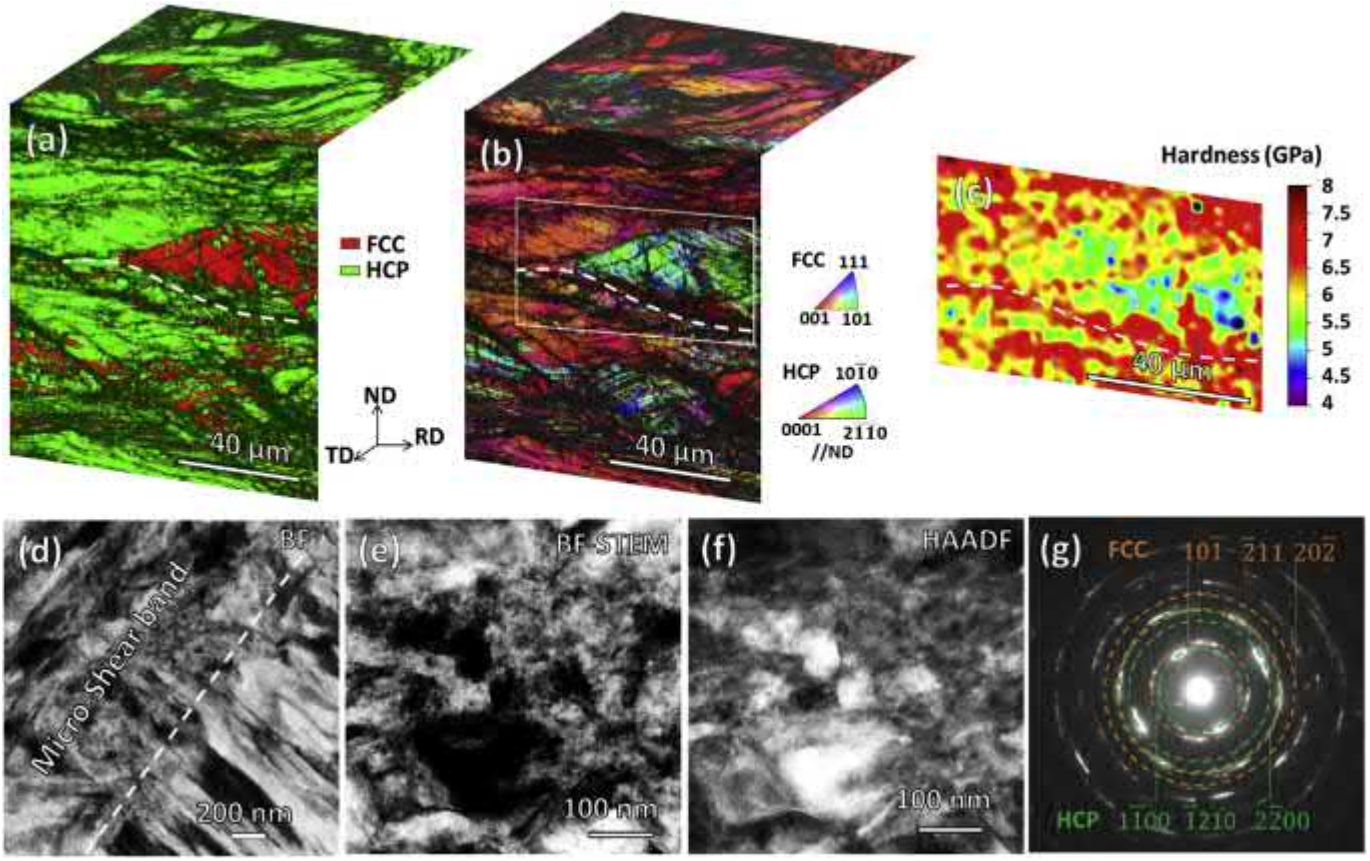

Fig. 5. As-rolled microstructure at a thickness reduction of 67%. (a) and (b) Psuedo-3D phase map and IPF map; (c) Nano-indentation map of the rectangular region in (b); (d) Bright field (BF) image showing nanostructures in the micro-shear bands; (e) and (f) Enlarged BF image and high-angle annular dark field (HAADF) image of nano-grains; (g) Selected area diffraction patterns (SADP) in the micro-shear bands showing both FCC and HCP phases.

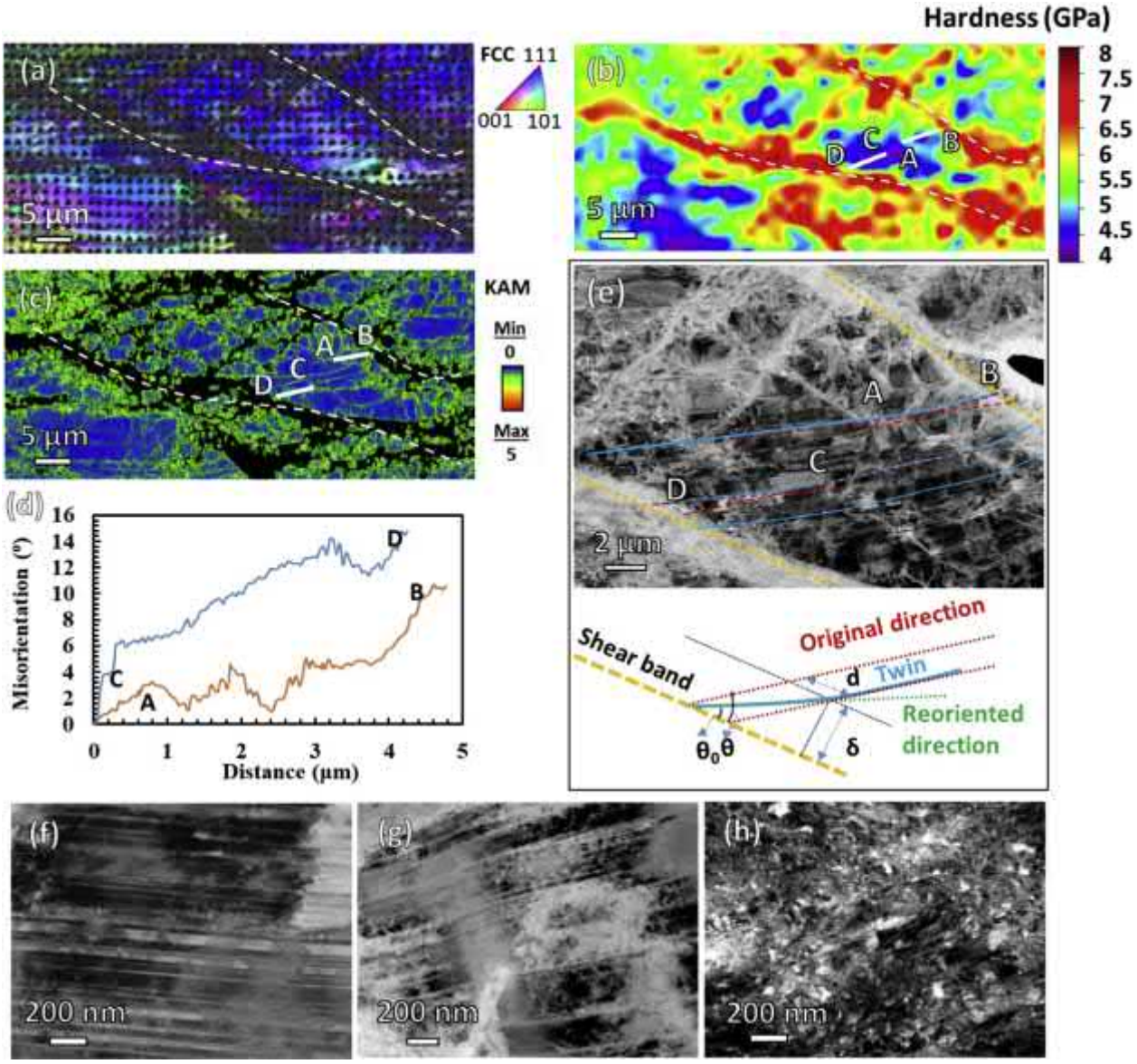

Fig. 6. (a) IPF map of the tempered specimen with preceding rolling reduction of 67%; (b) Nano-indentation map showing gradient hardness values; (c) KAM map; (d) Misorientation profiles from A to B and from C to D showing the increase of misorientation angle from the grain interior to shear bands. (e) ECC image and schematic illustration plot of bended twin lamellae due to localized shear strain. (f), (g) and (h) ECC images revealing the grain interior with nanotwins, the region adjacent to the shear bands with a high density of dislocations, and the shear bands containing nanocrystals, respectively.

For the tempered specimen with preceding rolling reduction of 34%, deformation-induced HCP martensitic transformation occurs at a local strain of 10% under tensile loading. The HCP lamellae are found along the pre-existing twin boundaries (Fig. 9b). With increasing the local strain to 40%, i.e. inside the necking area (Fig. 8d), a slightly higher volume fraction of HCP martensite is found (from 3.8 vol % to 4.7 vol %) (Fig. 9c). Fig. 9d shows the twin boundary length per unit area and the volume fraction of HCP martensite versus local strain. Also, the twin fraction increases upon loading.

4. Discussion

4.1. Deformation-driven bidirectional martensitic transformation

4.1.1. Bidirectional transformation at intersections of two HCP lamellae

At a low cold rolling thickness reduction of 14%, the forward deformation-induced martensitic transformation from the FCC matrix to the HCP martensite is dominant and multiple HCP variants are activated along the {111} planes (Fig. 1). The forward martensitic phase transformation obeys the S-N relationship, i.e. $\{111\}_{FCC}//\{0001\}_{HCP}$ and $<10\bar{1}>_{FCC}//<11\bar{2}0>_{HCP}$ [24]. Interestingly, reversely transformed fresh FCC phase is found at the intersections of two crossing HCP lamellae. Fig. 10a shows that the new FCC phase exhibits a misorientation angle of 60° with respect to the FCC matrix (from point A to point B), i.e. a twin relationship. Moreover, the new HCP variant forms adjacent to the reverted FCC phase and along HCP-2 lamellae (pointed by a white arrow in Fig. 10b_1). The formation of the new HCP variant at the intersecting regions of the two initial HCP bands has also been reported in high-interstitial-alloyed austenitic steels [18] and shape memory alloys [25,26]. It has been explained in terms of the cooperative shear associated with the initial two HCP variants [25,26]. There are 12 possible HCP variants relative to an FCC host phase according to the

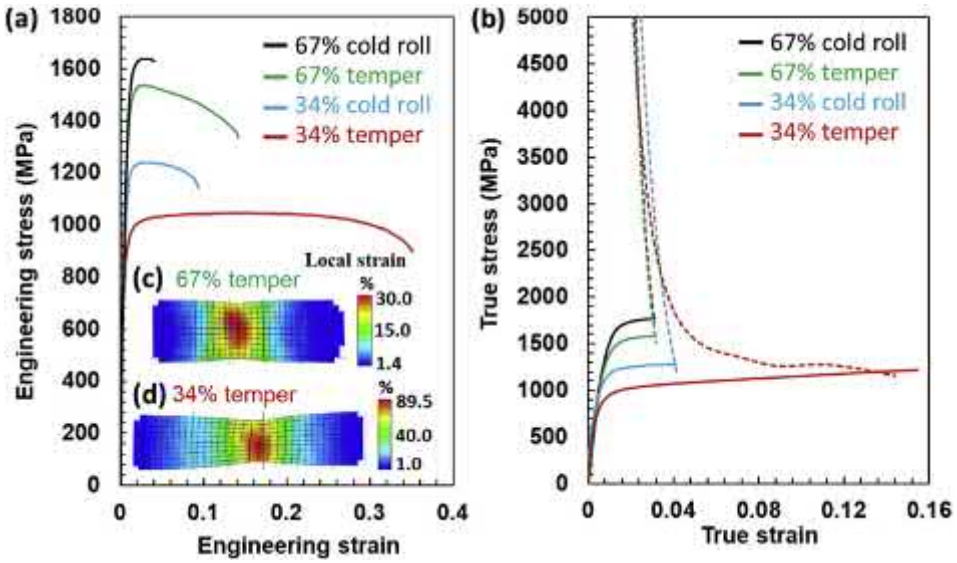

Fig. 7. (a) Engineering stress-strain curves of the as-rolled specimens at thickness reductions of 34% and 67% as well as of the tempered specimens; (b) True stress-strain plots (solid lines) and work hardening curves (dashed lines); (c) and (d) are local strain maps right before fracture of the two tempered specimens with preceding rolling reductions of 34% and 67%, respectively.

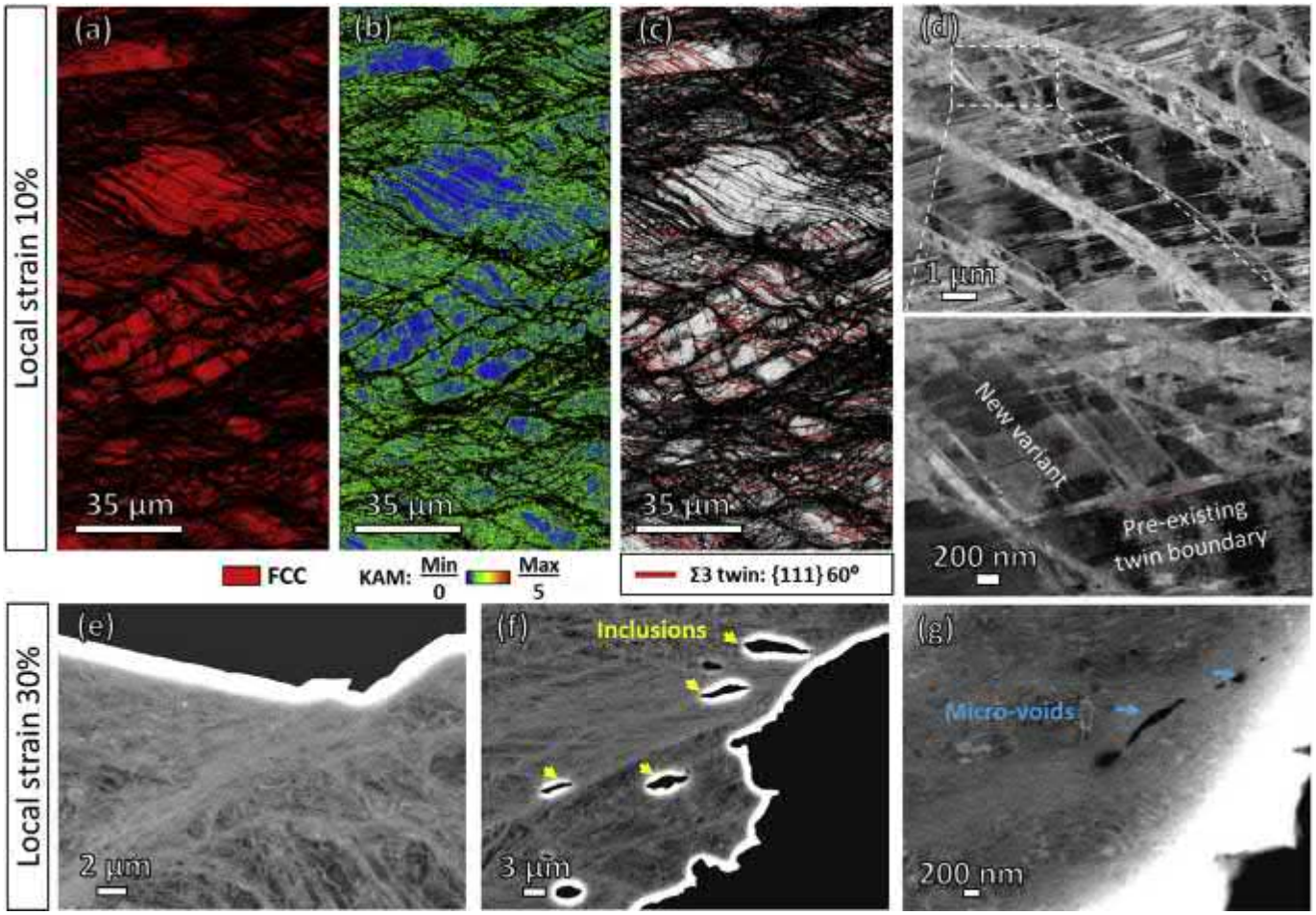

Fig. 8. Deformation microstructures of the tempered 67% rolled specimen upon tensile loading at local strains of 10% (a)–(d) and 30% (e)–(g). (a) Phase map; (b) IPF map; (c) IQ map superimposed with twin boundaries; (d) ECC images showing new twin variants. ECC images revealing (e) necking steps along the edge of the tensile specimen, (f) cracks along the shear bands at the fracture surface, and (g) micro-voids form inside the shear bands.

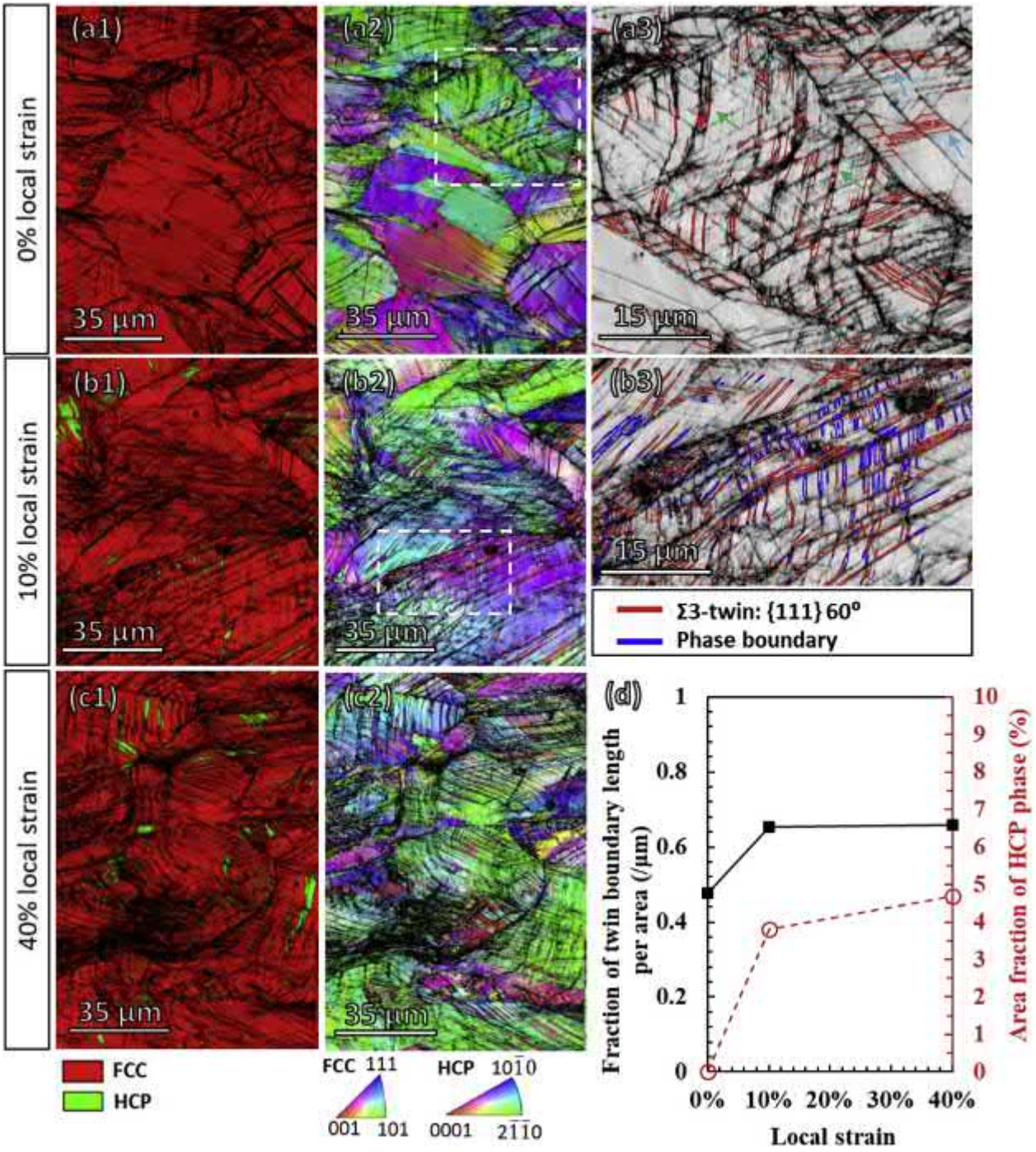

Fig. 9. Deformation microstructures of the tempered 34% rolled specimen during tensile testing at local strains of (a) 0%, (b) 10%, and (c) 40%, where (1) refers to phase maps, (2) IPF maps, and (3) enlarged IQ maps superimposed with twin and phase boundaries. (d) The fraction of twin boundary length per unit area (μm/μm^2) and the volume fraction of HCP martensite versus local strain.

12 shear systems {111} ⟨11$\bar{2}$⟩. Nevertheless, only 4 orientations of the HCP phase are distinguishable due to the symmetry of the hexagonal crystal [25,26]. By TEM analysis, 6 rotation relationships of the HCP variants are generally accessible, i.e., 19.5°, 31.5°, 39°, 51°, 70.5° and 90° via rotation of the basal plane [27]. In Fig. 10$b_{1\text{-}4}$, the misorientation angle between HCP-1 and HCP-2 is around 70.5°, while the angles of the new HCP variant relative to HCP-1 and HCP-2 are 19.5° and 90°, respectively. This, in turn, confirms that the formation of the new HCP phase is related to the generation of a new variant of stacking faults and their rearrangement due to the local stress state.

It is known that the formation of twins and HCP martensite in the FCC matrix both involve $\frac{1}{6}<11\bar{2}>$ Shockley partial dislocations [28,29]. The FCC twin is formed by the passage of partial dislocations on successive {111} planes, while the HCP phase is generated by passing partial dislocations on every second {111} plane [28,29]. It is noted that the FCC Shockley partial dislocation with a Burgers vector of ⟨11$\bar{2}$⟩ on the {111} plane is equivalent to the partial

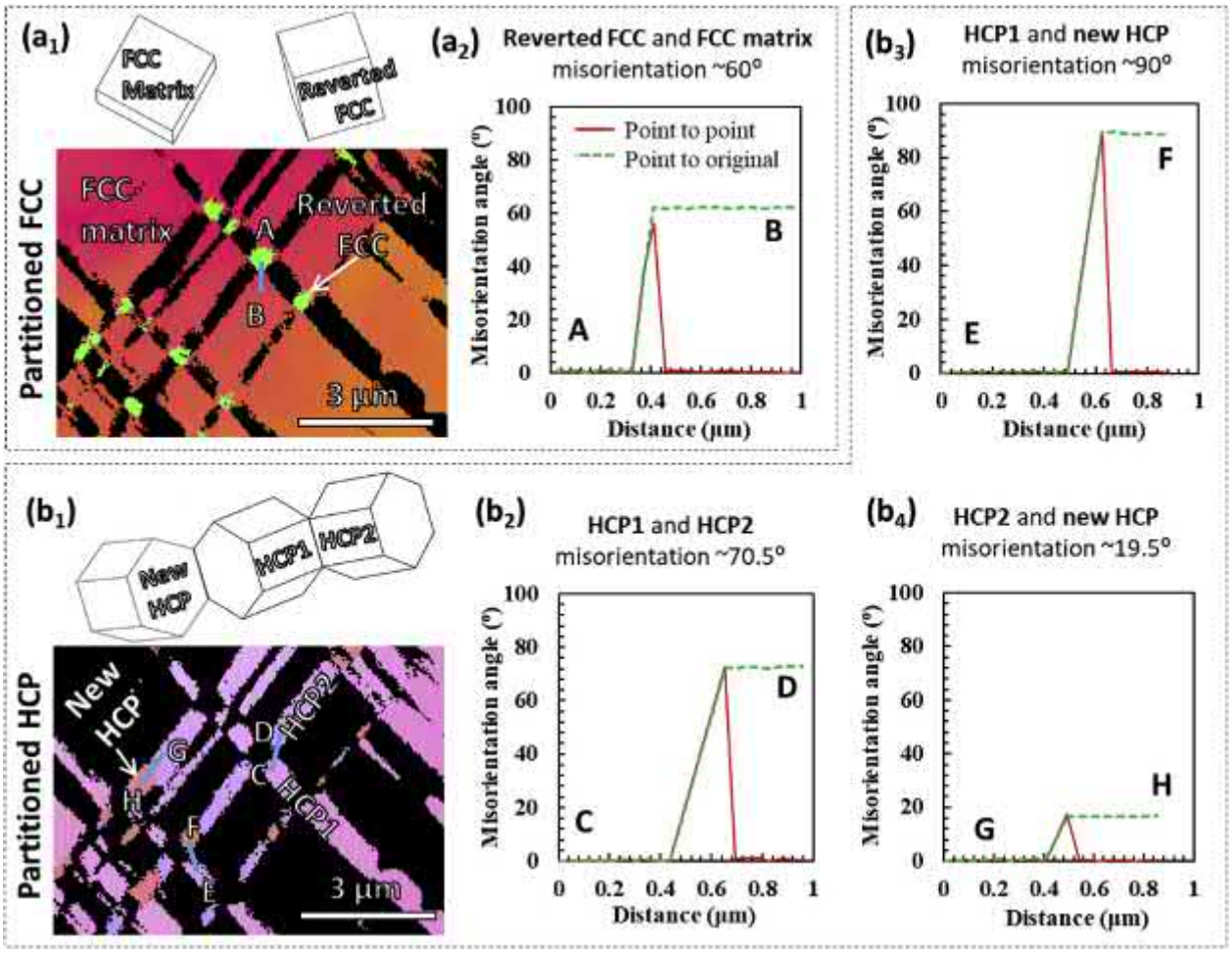

Fig. 10. Microstructure and misorientation relationship of two-crosshatched HCP lamellae and reverted FCC in the 14% rolled specimen. Partitioned IPF maps of (a_1) FCC phase and (b_1) HCP phase; Misorientation profiles of (a_2) reverted FCC phase and FCC matrix, (b_2) HCP-1 and HCP-2, (b_3) HCP-1 and new HCP variant, and (b_4) HCP-2 and new HCP variant.

dislocation with Burgers vector $<10\bar{1}0>$ on the {0001} basal plane of the HCP phase. Typically, the formation of a twin band leads to a homogeneous simple shear with a shear angle of 39° on the conjugated {111} plane about the <011> axis [25,26]. However, the formation of a single HCP variant results in an average shear angle of 19.5°, which is half of the twinning shear. This, in turn, results in the rotation of the conjugated {111} plane to a new position of 90° with respect to the {0001} basal plane of the HCP variant [25,26]. When two conjugated HCP variants are initiated (70.5° between HCP-1 and HCP-2), they could possibly pass through each other [25,26]. According to Yang and Wayman [25,26], the intersection of the two crossing HCP variants creates a rigid-body-rotation zone arising from the overlap of the displacement gradients imposed by the two initial HCP variants, which leads to a full FCC twinning shear. This is consistent with the orientation relationships shown in Fig. 10a. Yet, the so reverted FCC phase region is also mechanically metastable, thus a new HCP variant can form when locally sufficiently stressed.

In shape memory alloys (Fe-13.7Mn-6Si-8.3Cr-4.9Ni) [27], stainless steels [30] and high Mn- steels [21,22], BCC/BCT-martensite and/or new HCP variants formed at intersections of two crossing HCP martensite lamellae. This effect was explained in terms of the additive shear contributions of the two intersecting HCP lamellae. Yet, different from these earlier findings, in the current iHEA, only HCP and reverted FCC phases are found upon deformation, but no BCC or BCT-martensite was detected, neither in regions where HCP lamellae intersect nor anywhere else. This is ascribed to the much higher driving force required to form the BCC/BCT phase [31]. It has been reported in Fe-(15-30 at. %)Mn and Fe-Mn-C alloys that Mn affects the local magnetic moment, thus the phase transformation from the antiferromagnetic FCC phase to the ferromagnetic BCC phase is inhibited in these materials [32,33].

4.1.2. Deformation kink bands and formation of reverted FCC phase

At a thickness reduction of 26%, the volume fraction of HCP martensite (~60 vol %) is about three times higher than that at 14% reduction. With further rolling deformation (34% and 67%), the amount of HCP phase remains constant. This is ascribed to the metastability of both the FCC and the HCP phases and the simultaneous forward and reverse martensitic transformations upon deformation. In the reverted FCC phase, partial dislocations and stacking faults have readily formed (Figs. 1e and 2e), which are known as the sources for the formation of the HCP phase [28,29]. In fact, the new HCP variant has been observed in the reverted FCC phase (Fig. 2 c_2 and c_3). Thus, the reverted FCC phase is also considered mechanically metastable. From a thermodynamics point of view, the occurrence of such bidirectional transformations is due to the relatively low energy barrier between the FCC and the HCP phases [34]. The eigenstress field created by cold working as well as its spatial inhomogeneity appears to be sufficiently high to overcome such small energy barriers. From a dynamic displacive phase transformation perspective, both, forward and reverse

martensitic transformations are related to the generation and motion of partial dislocations and their reconstructions according to the local stress state.

As shown in Fig. 3f, the HCP grains exhibit a near-basal texture. This is a typical rolling texture in HCP metals due to the preferential activation of basal slip. The current HCP phase possesses a c/a ratio of 1.618 (a = 2.54 Å and c = 4.11 Å according to XRD analysis), i.e. a value close to the ideal value (1.633) derived for hard sphere stacking. In such cases, the critical resolved shear stress (CRSS) for activating basal slip is much lower than those required for non-basal slip activation [35]. In Fig. 3f, the {0001} basal texture component is tilted by ~10° due to grain-interaction and the activation of non-basal slip. Fig. 4a and b reveal basal, prismatic, as well as pyramidal I and II slip traces, identified by EBSD and ECCI analysis. Multiple deformation kink bands also develop along the pyramidal habit planes $\{11\bar{2}2\}$ and $\{10\bar{1}1\}$ of the HCP phase (Figs. 2 and 3). Development of deformation kink bands was reported in a $Mg_{85}Zn_6Y_9$ alloy containing long period stacking ordered (LPSO) phase [36]. The interactions of the deformation bands with the LPSO structures leave behind a large number of lattice defects, which can activate other slip systems and cross slip, resulting in the kink deformation [36]. Stacking faults in the Mg-Zn-Y alloys with LPSO phase also play an important role in stimulating pyramidal slip providing non-basal texture components [28].

In the current study, reverted FCC phase together with new HCP variants are detected among the deformation kink bands. To understand the mechanisms of the deformation-driven reverse transformation from the HCP martensite into the FCC phase, the substructures of the 34% rolled specimen have been analyzed by high-resolution (HR)-TEM (Fig. 11). The bright field (BF) and dark field (DF) images show alternating layers of deformation-induced HCP phase and FCC phase with dislocation structures and stacking faults (Fig. 11a and b). The selected area diffraction patterns (SADP, Fig. 12c) reveal prior FCC phase, HCP martensite and reverted FCC phase, showing the following crystallographic relationships: $\{\bar{1}1\bar{1}\}_{Prior\ FCC}//\{0001\}_{HCP}//\{001\}_{Reverted\ FCC}$ and $<110>_{Prior\ FCC}//<11\bar{2}0>_{HCP}//<100>_{Reverted\ FCC}$

In the HR-TEM images (Fig. 12d and e), stacking faults can be seen in both, the deformation-induced HCP martensite and the reverted FCC phase. Fig. 12f shows a stacking fault at the interface of the deformation-induced HCP phase and the reverted FCC phase. Such a stacking fault on the basal plane, i.e. the close-packed plane, of the HCP phase (AB sequence) is equivalent to an atomic layer of the FCC phase (ABC stacking) [34]. On the one hand, the HCP martensite and the FCC atomic layer follow the S-N relationship [24], which has also been confirmed by SADP (Fig. 12c). On the other hand, the reverted FCC phase exhibits a misorientation angle of 60° about the {111} plane with respect to the prior FCC atomic layer, which is a twin relationship. The reverted FCC phase displays a CBA stacking sequence. The deformation-induced reverse martensitic transformation from HCP to FCC phase has been found in shape memory steels [37] and high Mn TRIP steels [22,38], where stacking faults pre-exist in the HCP martensite forming a long period ordering (LPO) structure. Kwon et al. [22] found that the pre-existing stacking faults in a 6H LPO structured HCP phase are responsible for the reverse martensitic phase transformation.

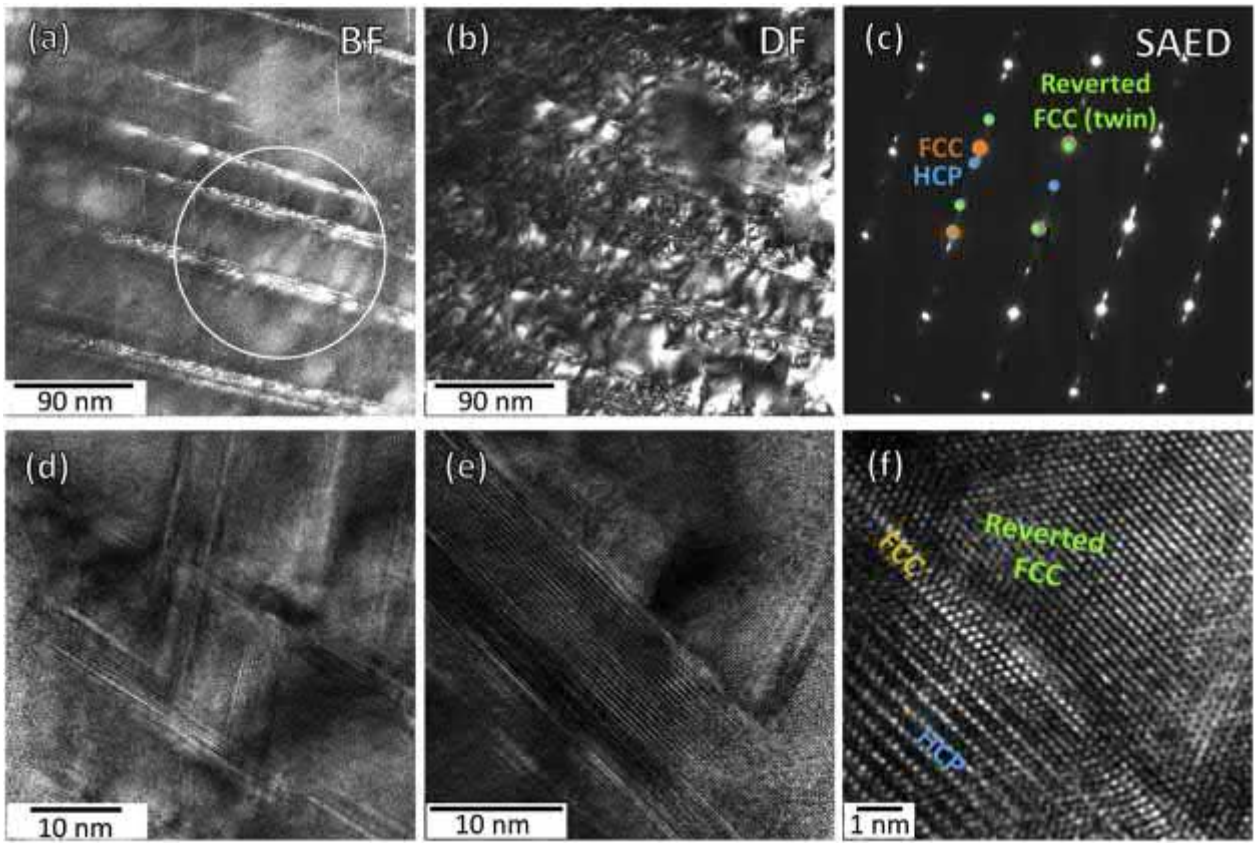

Fig. 11. Details of the substructure of the 34% rolled specimen. (a) BF image and DF image revealing alternating layers of HCP martensite and reverted FCC phase; (c) Selected area diffraction (SAD) pattern of the circled region illustrating the crystallographic orientation relationship of prior FCC, HCP martensite and reverted FCC phase. (d) and (e) HR-TEM images showing stacking faults in both HCP phase and reverted FCC phase; (f) Atomic resolution image showing an FCC atomic layer at the interface of HCP martensite and reverted FCC phase.

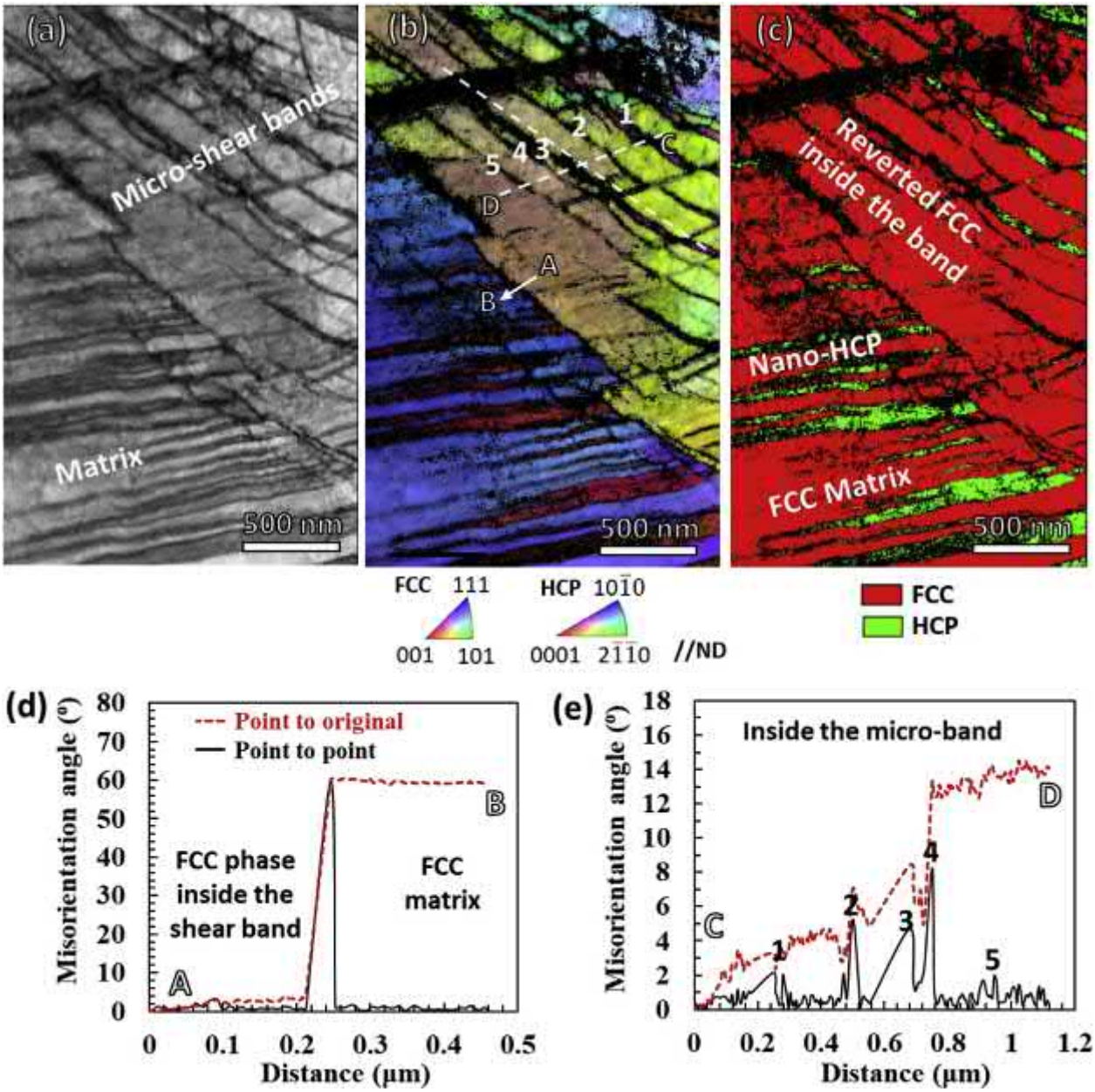

Fig. 12. Transmission-EBSD microstructures of the 34% rolled specimen. (a) IQ map; (b) IPF map revealing substructure inside micro-shear bands; (c) Phase map showing nano-layers of HCP martensite in FCC matrix and formation of reverted FCC phase inside the bands. Misorientation profiles (d) between the FCC matrix and the reverted FCC phase in the band, and (e) in the vicinity of the micro-shear band.

Kajiwara [37] suggested that the FCC phase that formed in the HCP martensite is prone to arrange an ABC stacking order, which progresses by creating a dislocation loop on every third layer in order to reduce the repulsive force between neighboring partials. In contrast, the CBA stacking sequence (FCC twin) requires the formation of a dislocation loop on every layer for generating stacking faults on every {111} plane, which is unlikely to occur.

The interactions of deformation kink bands with pre-existing stacking faults in the HCP lamellae are observed in Fig. 2d and e. This can lead to additional shear of the HCP phase and the dissociation of full dislocations, thus generating new partial dislocations to form reverted FCC phase. It has been reported in HCP alloys that the <c+a> pyramidal II dislocations $\{11\bar{2}2\}\ <11\bar{2}3>$ can dissociate into two concentric $1/6<20\bar{2}3>$ type partial dislocations with a basal stacking fault [39]. Angnew et al. [40] suggested that the <c+a> pyramidal I slip $\{10\bar{1}1\}\ <11\bar{2}3>$ could decompose into <c> and <a> dislocations to reduce the associated elastic energy, where <a> dislocations further extend on the basal plane and constrain a basal stacking fault. Therefore, the interactions of pyramidal slip and pre-existing stacking faults can lead to dissociation of full dislocations and the generation of new Shockley partials that are the sources for the formation of reverted FCC phase, as discussed above. Also, in the HCP structure, the perfect <*a*> Burgers vector is $\mathbf{b} = \frac{1}{3}[11\bar{2}0]$, normally located on a basal {0001} plane and a prismatic $\{10\bar{1}0\}$ plane [41]. When a stable I_2 stacking fault exists on the basal plane, the dislocation dissociates on the basal plane into two Shockley partial dislocations bounding a stacking fault ribbon, which is similar to the well-known dissociation process of $\langle 10\bar{1}\rangle\ \{111\}$ slip in FCC [41]. The Burgers vector reaction of <*a*> slip follows the vector equation

$\frac{1}{3}[11\bar{2}0]^{(0001)} \rightarrow \frac{1}{3}[10\bar{1}0]^{(0001)} + \frac{1}{3}[01\bar{1}0]^{(0001)}$ [41]. In accordance with the local shear stress, the multiplication of Shockley partials on every layer of the close-packed plane of the HCP phase leads to the formation of an FCC twin.

Tension twins (89° and $\{11\bar{2}0\}$) are found inside the HCP martensite, but contraction twins or secondary twins are rarely observed. The HCP phase exhibits a near-basal orientation where the c-axis of the HCP crystal is primarily subjected to compression during rolling. It is known that tension twins normally occur when the c-axis is subjected to tension stress, while contraction twins form under compressive loads along the c-axis [42]. Thus, the HCP martensite with such an orientation is unfavorable for activating tension twins according to the Schmid law. Yet, we observed tension twins in the HCP lamellae among the deformation bands (Fig. 2c) and close to grain/phase boundaries (Figs. 3e and 4i). Also, pyramidal slip traces were found near tension twins (Fig. 4c). This can be related to the activation of pyramidal dislocations $\{11\bar{1}01\}\langle 11\bar{2}3\rangle$, a mechanism which might facilitate formation of tension twins on the $\{1\bar{1}02\}$ habit plane. This phenomenon has also been reported in HCP Mg alloys where the tension twins appear in unfavorably oriented grains together with a few dislocations with Burgers vectors containing a *c*-component (e.g., $\mathbf{b} = [c]$ or $<c + a>$) [42].

4.1.3. Nanostructure development inside of micro-shear bands

To unveil the mechanism of the formation of nano(sub)grains inside the micro-shear bands, transmission-EBSD has been applied on the sample rolled to 34% thickness reduction (Fig. 12). The micro-shear band consists of multiple fine slip bands (e.g. marked as 1-5 in Fig. 12b) mainly along two directions (indicated by dashed lines in Fig. 12b) that segment the micro-shear band into nanosized cells (100–500 nm). The reverted FCC phase forms in the micro-shear band and exhibits a twin misorientation angle of 60° with respect to the FCC matrix (Fig. 12c and d). The misorientation angles among each slip band in the vicinity of the micro-shear band are around 2-8° (Fig. 12e), i.e. constituting low angle grain boundaries. This means that elongated nano-subgrains gradually develop inside the bands. With further increasing rolling strain, the elongated subgrain interfaces accumulate more dislocations, evolving into dual-phase equiaxed nano-crystals (Fig. 5g).

4.1.4. Effect of local dissipative temperature increase on phase transformation

Strain-induced reverse martensitic phase transformation from the HCP to the FCC phase is known in Co [14] and its alloys [15]. In pure Co, the two phases mix close to the allotropic transformation point [14]. During ball milling of pure Co, strain-induced martensitic phase transformation from FCC to HCP and reverse transformation from HCP to FCC has been observed, achieving eventually single-phase FCC structure [14]. Reverse martensitic phase transformation was also reported in nanocrystalline Co-Ni alloys during tensile testing [15].

As such phase transformation effects have been explained in terms of adiabatic heating, we estimated the macroscopic temperature increase also for the current case (see Appendix A, Fig. 14a). At a low reduction of 14% (true strain 15%), the increase in temperature due to plastic deformation is around 15 °C. At 67% (true strain 110%), the temperature rise is estimated to be ~276 °C without considering temperature losses between the rolling passes. Yet, for the current iHEA, thermally induced reverse transformation from HCP to FCC phase is observed in a temperature range of 380–420 °C by dilatometry (see Appendix B, Fig. 14b). Note that the local temperature increase due to the concentrated deformation could be higher than the overall temperature increment of the specimen as a whole. However, it is clear that the formation of the reverted FCC phase shows a displacive transformation characteristic following a coherent crystallographic relationship with the HCP phase. Also, the reverted FCC phase forms a twin relationship with the FCC matrix, which is basically different from thermally induced reverse transformation where the HCP phase transforms back to the parent FCC phase [43,44]. Since we find deformation-driven reverted FCC phase already at a very low strain of 15% for the current alloy, i.e. without any substantial temperature increase, we conclude that the specific local stress conditions are more important for reversion than the local temperature increase.

4.2. Hierarchical nanostructure formation upon tempering

Upon tempering at 400 °C for 10 min, HCP martensite thermally reverts into FCC phase adopting the S-N relationship [24]. The interface between the thermally induced reverted FCC phase and the deformation-induced reverted FCC phase is identified as a twin boundary. This is due to the fact that the deformation-induced reverted FCC lamellae exhibit a twin relationship with the pre-existing FCC nano-layers, while the thermally induced reverted FCC follows the same stacking sequence as the prior FCC nano-layers.

The nanocrystals in the micro-shear bands have the highest hardness value observed in these microstructures due to the severe local grain refinement (Fig. 5c). APT analysis has been additionally conducted in the vicinity of these features to analyze effects associated with local chemical composition fluctuations (Fig. 13 in Appendix). The results show substantial carbon enrichment in these shear bands due to the higher dislocation and interface density, providing multiple trapping sites. The carbon concentration at some of these defects is around 1.0 at. %, i.e. twice higher than at comparable features outside of these bands (Fig. 13c). The decoration kinetics is attributed to the enhanced dissipative heating that is associated with the formation of such shear bands [45]. The segregation of carbon also contributes to the ultra-high hardness of the micro-shear bands [46,47]. The substitutional elements Fe, Mn, Co, and Cr are distributed homogeneously.

Development of micro-shear bands results in the increase of the local shear strain. As schematically shown in Fig. 6e, the associated local shear strain can be described by the following equation [16].

$$\gamma = \frac{d}{\delta} = ctg\ \theta - ctg\ \theta_0 \tag{1}$$

where θ_0 is the original angle of the twin lamellae with respect to the shear band, θ is the reoriented angle of the bent portion of the lamellae, δ is the width of a unit segment (perpendicular to the shear direction) and d is the shear displacement of the unit segment [16]. In the present case, the average shear strain caused by shear banding (with a thickness of 2 μm) is around 1.8–2. The large lattice rotation caused by the micro-bands leads to an opposite rotation in regions adjacent to the bands. Hence, numerous submicron-sized dislocation cells (200–500 nm) form near the micro-shear bands, collecting the geometrically necessary dislocation (GND) content required to accommodate the large local shear strains and rotations (Fig. 6f and g). This is consistent with the hardness gradients found in these regions (Fig. 5c).

4.3. Relationship between nanostructure and mechanical response

The tempered specimen with a pre-rolling reduction of 67% exhibits a larger fraction of micro-shear bands containing nano-grains (35 vol % vs. 10 vol %) compared to the specimen reduced to 34%. The former material exhibits a higher YS (1.3 GPa) compared to the latter (900 MPa) owing to grain refinement strengthening.

However, the ductility of the tempered specimen with pre-rolling reduction of 34% is profoundly improved (total elongation increases from 14% to 30%), while maintaining a high UTS value (1.05 GPa). This is due to the enhancement of the work hardening rate by activating both, transformation-induced plasticity (TRIP) and twinning-induced plasticity (TWIP) in the 34% rolled and tempered specimen. Also, the larger space between the pre-existing nano-twins accumulates more dislocations and promotes more intense dislocation-twin interactions, contributing to work hardening [48]. The HCP martensite lamellae mainly develop along the pre-existing twins, since these twin boundaries act also as glide planes for partial dislocations that are necessary to facilitate HCP martensitic transformation [12]. For the 67% rolled and tempered specimen, the HCP martensitic transformation is largely inhibited due to the much smaller spacing of the pre-existing nano-twins. The fraction of mechanical twin is more or less the same before tensile loading and at the local strain of 10%, indicating that the contribution of TWIP is also limited. Micro-voids and cracks propagate along the micro-shear bands leading to early necking (Fig. 8e–g). Thus, the work hardening rate is not sufficiently high to compensate the localized deformation along the shear bands. This suggests that tuning of the bidirectional transformation and twinning behavior by cold rolling and tempering is important to obtain optimized nanostructures for a good strength-ductility combination, such as here realized in the 34% rolled and tempered iHEA.

5. Conclusions

As a result of this study, we propose a novel perspective of producing bulk nanostructured materials with superior mechanical properties by utilizing deformation-driven bidirectional phase transformation. This can be achieved by taking a design approach of tuning the materials' stacking fault energy close to their thermodynamic stability limits to trigger sequential forward and reverse athermal phase transformations upon loading. With the huge solid solution compositional space offered by the non-equiatomic HEA concept, the current iHEA has been developed to reach and utilize such metastability ranges. The resulting deformation mechanisms acting during deformation are summarized as follows.

1. At low cold rolling thickness reductions below 14%, deformation-induced forward HCP martensitic transformation is dominant in the single FCC matrix. At the intersections of two crossing HCP lamellae, deformation-induced reversed FCC phase forms. This is due to the additive shear contributions of the two intersecting HCP lamellae.
2. At medium reductions (26–34%), multiple deformation kink bands develop mainly on the pyramidal habit planes of the HCP martensite, among which deformation-induced reverted FCC phase and a new HCP variant form. This is related to the underlying dislocation reactions and rearrangement of the partial dislocations according to local stresses. The reverted FCC phase regions exhibit a twin stacking sequence relative to the prior FCC matrix. This, in turn, leads to a dual-phase nano-laminated structure.
3. At a higher thickness reduction of 67%, deformation bands grow into micro-shear bands where elongated subgrains gradually turn into equiaxed nanocrystals, facilitated by the large lattice rotation caused by shear banding.
4. Upon tempering of the 34% and 67% rolled specimens, single FCC phase nanostructures emerge, characterized by nanocrystals and nano-twins. An excellent strength-ductility synergy is achieved in tempered specimens with preceding-rolling reduction of 34%, owing to the improvement in the work hardening rate by joint activation of both TRIP and TWIP.

Acknowledgements

The financial support of the German Research Foundation (Deutsche Forschungsgemeinschaft, DFG) within the Priority Programme 2006 (Compositionally Complex Alloys – High Entropy Alloys) is acknowledged. The authors would like to gratefully acknowledge Dr. Seok Su Sohn and Dr. Jiali Zhang for discussion and the kind support of David Mayweg, M. Nellessen, K. Angenendt, M. Adamek, H. Bögershausen and B. Breitbach at Max-Planck-Institut für Eisenforschung.

Appendix

A. Calculation of the local dissipative temperature increase due to plastic deformation

The temperature increase due to plastic deformation upon cold rolling can be estimated by the following equation (2) [20].

$$\Delta T = \frac{\beta}{\rho C_V}\int_{\varepsilon_1}^{\varepsilon_2} \sigma d\varepsilon \tag{2}$$

where $\beta = 0.9$ (assuming 90% of the deformation work is converted to heat), ρ is the density of the iHEA (7.66 g/cm^3) and C_V is the specific heat capacity (~0.50 J/(g·K) for 304 stainless steel). σ is the average stress applied upon two rolls and ε is the effective strain.

The flow stress upon cold rolling, σ, can be estimated by Equation (3).

$$\sigma = \left(\frac{\dot{\varepsilon}}{\dot{\varepsilon}_{eq}}\right)^m \frac{K\varepsilon^n}{n+1} \tag{3}$$

Where $\dot{\varepsilon}$ is the true strain rate during tensile testing (0.001/s), $\dot{\varepsilon}_{eq}$ is the equivalent (true) strain rate during cold rolling, and m is the strain rate sensitivity (SRS) factor. The SRS factor (m=0.0067 MPa/s) is derived by plotting $log\sigma$ *vs.* $log\dot{\varepsilon}$ at strain rates ranging from 2.5×10^{-5} to 5×10^{-3} /s. This value is consistent with those reported in TRIP steels [49, 50] and a TRIP-assisted high entropy alloy [51]. It has been reported that the SRS values slightly increase (~0.01 MPa/s) at the strain rate above 1/s [49, 50]. Although the SRS value attained in the current case is in the quasi-static loading regime, it has a good agreement with those reported in TRIP steels at a broader range of strain rates from 3×10^{-3} /s to 100 /s under dynamic tensile testing [50]. The parameters K and n are calculated by plotting $log\sigma$ *vs.* $log\varepsilon$ using the room temperature tensile curve.

The equivalent strain rate during cold rolling can be calculated by Equation (3).

$$\dot{\varepsilon}_{eq} = \frac{0.1209Nln(H/h)}{\alpha} \tag{4}$$

Here, N is the peripheral speed, H and h are the initial and final height of the plate, and α is the contact angle, given by $\alpha = cos^{-1}\left(1 - \frac{H-h}{2R}\right)$, where R is the radius of the roll. In the current study, the rolling speed is 25 cm/s and each pass reduction is about 10%. the average strain rate for each pass is about 20/s. According to equations (2)-(4), the increase in temperature due to plastic deformation at different reductions is calculated without considering temperature loss between each pass and is shown in Fig. 14a.

B. Measurement of the thermal-induced reverse phase transformation temperature

The temperature of the reverse martensitic phase

transformation from the deformation-induced HCP martensite to FCC phase upon heating is measured by a dilatometer. Fig. 14b shows the change of length versus temperature. The variation of the slope is an indication of the phase transformation. It is thus determined that the temperature of the thermally induced reverse phase transformation ranges from 380 °C to 420 °C.

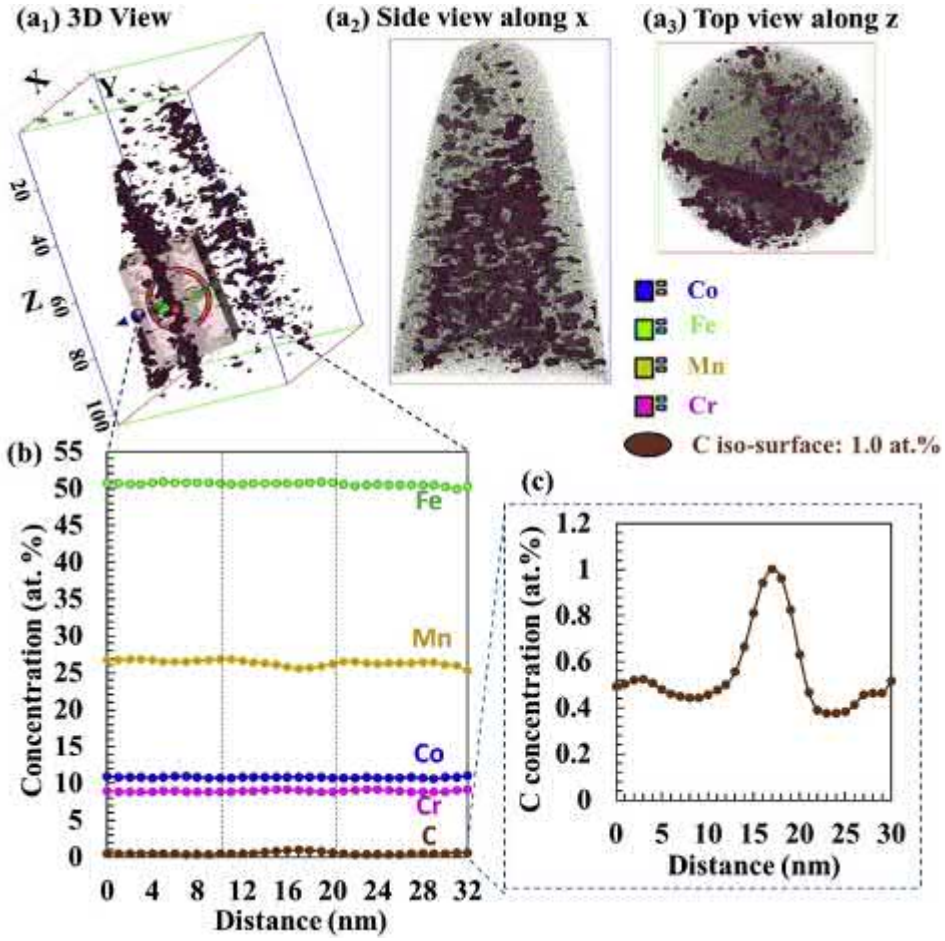

Fig. 13. APT analysis of the shear-banded region of the tempered 67% rolled specimen. (a) 3D view, 2D side view and top view of the tip with carbon iso-surface at 1.0 at.%; (b) Concentration profile of five elements; (c) Enlarged profile showing carbon concentration of ~1.0 at.% at some defects, i.e. twice higher than the surroundings.

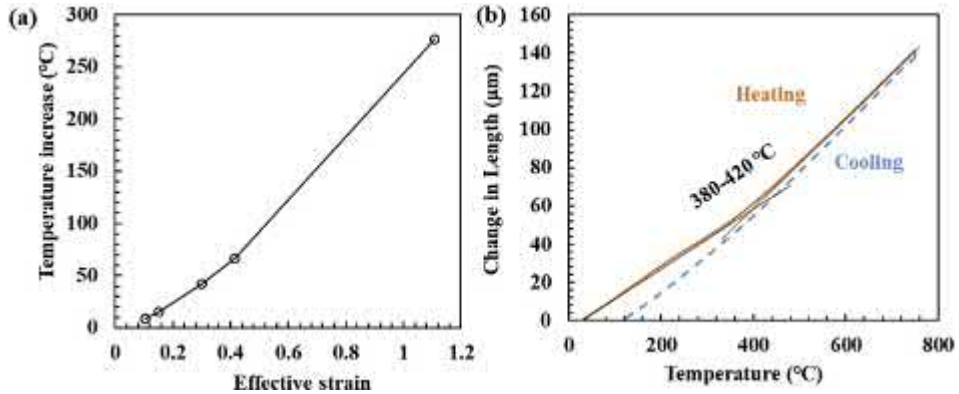

Fig. 14. (a) Increase of temperature due to plastic deformation at different reductions without considering the temperature loss between rolling passes; (b) Change in length of the as-cold-rolled specimen upon heating to 750 °C followed by cooling to room temperature measured by dilatometry.

References

[1] B. Cantor, I.T.H. Chang, P. Knight, A.J.B. Vincent, Mater. Sci. Eng., A 375–377 (2004) 213.
[2] J.-W. Yeh, S-Ka Chen, S.-J. Lin, J.-Y. Gan, T-Sh Chin, T.-T. Shun, C.-H. Tsau, S.-Y. Chang, Adv. Eng. Mater. 6 (2004) 299.
[3] Z. Li, K.G. Pradeep, Y. Deng, D. Raabe, C.C. Tasan, Nature 534 (2016) 227.
[4] Z. Li, D. Raabe, JOM 69 (2017) 2099.
[5] Z. Li, F. Kormann, B. Grabowski, J. Neugebauer, D. Raabe, Acta Mater. 136 (2017) 262.
[6] Z. Li, C.C. Tasan, H. Springer, B. Gault, D. Raabe, Sci. Rep. 7 (2017) 1.
[7] M. Wang, Z. Li, D. Raabe, Acta Mater. 147 (2018) 236.
[8] J. Su, D. Raabe, Z. Li, Acta Mater. 163 (2019) 40.
[9] E. Ma, T. Zhu, Mater. Today 20 (2017) 323.
[10] Y. Wang, M. Chen, F. Zhou, E. Ma, Nature (2002) 419.
[11] K. Lu, L. Lu, S. Suresh, Science 324 (2009) 349.
[12] K. Lu, Nat. Rev. Mater. 1 (2016) 1.
[13] L. Lu, X. Chen, X. Huang, K. Lu, Science 323 (2009) 607.
[14] X.C. Liu, H.W. Zhang, K. Lu, Science 342 (2013) 337.
[15] F.K. Yan, G.Z. Liu, N.R. Tao, K. Lu, Acta Mater. 60 (2012) 1059.
[16] C.S. Hong, N.R. Tao, X. Huang, K. Lu, Acta Mater. 58 (2010) 3103.
[17] T. Morikawa, D. Senba, K. Higashida, R. Onodera, Mater. Trans. JIM 40 (1999) 891.
[18] T.-H. Lee, E. Shin, C.-S. Oh, H.-Y. Ha, S.-J. Kim, Acta Mater. 58 (2010) 3173.
[19] W. Lu, C.H. Liebscher, G. Dehm, D. Raabe, Z. Li, Adv. Mater. 1804727 (2018) 1.
[20] J. Su, M. Sanjari, A.S.H. Kabir, I.-H. Jung, J.J. Jonas, S. Yue, H. Utsunomiy, Mater. Sci. Eng., A 636 (2015) 582.
[21] J.-B. Seol, J.E. Jung, Y.W. Jang, C.G. Park, Acta Mater. 61 (2013) 558.
[22] K.H. Kwon, B.-C. Suh, S.-I. Baik, Y.-W. Kim, J.-K. Choi, N.J. Kim, Sci. Technol. Adv. Mater. 14 (2013) 1.
[23] G.B. Olson, M. Cohen, Metall. Trans. AMetall. Trans. A 7A (1976) 1905.
[24] G.B. Olson, M. Cohen, J. Less Common. Met. 28 (1972) 107.
[25] J.H. Yang, C.M. Wayman, Acta Metall. Mater. 40 (1992) 2025.
[26] J.H. Yang, C.M. Wayman, Acta Metall. Mater. 40 (1992) 2011.
[27] J.H. Yang, C.M. Wayman, Metall. Trans. AMetall. Trans. A 23A (1992) 1445.
[28] S. Mahajan, G.Y. Chin, Acta Metall. 21 (1973) 1353.
[29] S. Mahajan, M.L. Green, D. Brasen, Metall. Tran. A 8A (1977) 283.
[30] C. Herrera, D. Ponge, D. Raabe, Acta Mater. 59 (2011) 4653.
[31] A. Saeed-Akbari, J. Imlau, U. Prahl, W. Bleck, Metall. Mater. Trans. 40A (2009) 3076.
[32] H. Idrissi, L. Ryelandt, M. Veron, D. Schryvers, P.J. Jacques, Scripta Mater. 60 (2009) 941.
[33] N.I. Medvedeva, D.V. Aken, J.E. Medvedeva, J. Phys. Condens. Matter 22 (2010) 1.
[34] G.B. Olson, M. Cohen, Metall. Trans. AMetall. Trans. A 7A (1976) 1897.
[35] M.H. Yoo, S.R. Agnew, J.R. Morris, K.M. Ho, Mater. Sci. Eng. 319 – 321 (2001) 87.
[36] K. Hagihara, M. Yamasaki, M. Honnami, H. Izuno, M. Tane, T. Nakano, Y. Kawamura, Phil. Mag. 95 (2015) 132.
[37] S. Kajiwara, Mater. Sci. Eng. 273–275 (1999) 67.
[38] J.B. Seol, J.G. Kim, S.H. Na, C.G. Park, H.S. Kim, Acta Mater. 131 (2017) 187.
[39] J. Geng, M.F. Chisholm, R.K. Mishra, K.S. Kumar, Phil. Mag. 95 (2015) 3910.
[40] S.R. Agnew, J.A. Horton, M.H. Yoo, Metall. Mater. Trans. 33A (2002) 851.
[41] D. Hull, D.J. Bacon, Introduction to Dislocations, Elsevier Ltd., USA, 2011.
[42] S.R. Agnew, O. Duygulu, Int. J. Plast. 21 (2005) 1161.
[43] N. Bergeon, S. Kajiwara, T. Kikuchi, Acta Mater. 48 (2000) 4053.
[44] M.J. Lai, Y.J. Li, L. Lillpopp, D. Ponge, S. Will, D. Raabe, Acta Mater. 155 (2018) 222.
[45] S. Djaziri, Y. Li, G.A. Nematollahi, B. Grabowski, Shoji Goto, C. Kirchlechner, A. Kostka, S. Doyle, J. Neugebauer, D. Raabe, G. Dehm, Adv. Mater. 28 (2016) 7753.
[46] Y. Li, D. Raabe, M. Herbig, P.-P. Choi, S. Goto, A. Kostka, H. Yarita, C. Borchers, R. Kirchheim, Phys. Rev. Lett. 113 (2014) 1.
[47] D. Raabe, P.-P. Choi, Y. Li, A. Kostka, X. Sauvage, F. Lecouturier, K. Hono, R. Kirchheim, R. Pippan, D. Embury, MRS Bull. 35 (2010) 982.
[48] K. Lu, Nature Reviews Materials, vol. 1, 2016, p. 1.
[49] O. GraÈssel, L. KruÈger, G. Frommeyer, L.W. Meyer, Int. J. Plast. 16 (2000) 1391.
[50] H. Huh, S.-B. Kim, J.-H. Song, J.-H. Lim, Int. J. Mech. Sci. 50 (2008) 918.
[51] S. Basu, Z. Li, K.G. Pradeep, D. Raabe, Front. Mater. 5 (2018) 1.